Research article

Experimental analysis of free-standing and substrate-constrained Ga-doped ZnO nanostructured thermoelectric films

Aicha S. Lemine [a,b], Jolly Bhadra [b,c,*], Anton Popelka [c], Muni Raj Maurya [c],
Kishor Kumar Sadasivuni [c], Rana Abdul Shakoor [a,c], Ahmad Zubair [b,c],
Noora J. Al-Thani [b], Anwarul Hasan [a,d,**]

[a] Department of Mechanical and Industrial Engineering, College of Engineering, Qatar University, 2713, Doha, Qatar
[b] Qatar University Young Scientists Center (QUYSC), Qatar University, 2713, Doha, Qatar
[c] Center for Advanced Materials (CAM), Qatar University, 2713, Doha, Qatar
[d] Biomedical Research Center (BRC), Qatar University, 2713, Doha, Qatar

ARTICLE INFO

ABSTRACT

Developing thermoelectric films without substrates—free-standing films—eliminates substrate-induced effects on performance and meets the flexibility requirements of emerging wearable thermoelectric applications. This study investigates Gallium-doped Zinc Oxide (GZO), composed of abundant and non-toxic elements, to fabricate a substrate-free GZO film via 3D printing and compares its structural, chemical, and thermoelectric properties with those of a substrate-constrained GZO film produced through chemical deposition. Both films exhibited uniform crystal structures and phase purity; however, the substrate-constrained film displayed additional diffraction peaks, suggesting potential substrate interactions. The 3D-printed free-standing film effectively eliminated the tensile stresses observed in the substrate-constrained film. FE-STEM analysis revealed nanostructures with homogeneous elemental distribution in both films, though the substrate-constrained film showed discontinuities, such as pores, likely caused by post-deposition annealing treatment. XPS analysis highlighted differences in chemical states and elemental compositions between the films, influenced by fabrication methods, substrate-induced stresses, and surface energy mismatches. The free-standing GZO film developed through 3D printing exhibited a more balanced incorporation of Zn and O, as it was not subject to substrate or post-deposition annealing constraints. Consequently, it demonstrated a 14 % increase in electrical conductivity and a 91 % improvement in the Seebeck coefficient compared to the substrate-constrained film, resulting in a higher room-temperature power factor of 261 nW/m·K^2. These findings underscore the potential of 3D-printed free-standing GZO films to advance thermoelectric applications, offering a promising alternative to overcome the challenges of substrate-constrained films and further drive innovation in the field.

* Corresponding author. Department of Mechanical and Industrial Engineering, College of Engineering, Qatar University, 2713, Doha, Qatar.
** Corresponding author. Department of Mechanical and Industrial Engineering, College of Engineering, Qatar University, 2713, Doha, Qatar.
E-mail addresses: jollybhadra@qu.edu.qa (J. Bhadra), ahasan@qu.edu.qa (A. Hasan).

1. Introduction

Rapid industrialization and urbanization have significantly increased global energy consumption and environmental concerns [1]. Renewable and pollution-free ambient energy sources can reduce carbon dioxide (CO_2) emissions by 1.2 % for every 1 % increase in renewable energy use [1]. Thermoelectric (TE) technology, which converts low-grade thermal energy into high-grade electrical energy, holds great promise for sustainable energy harvesting and supporting a carbon-free economy [1]. TE technology is valued for its reliability, solid-state nature, noiseless operation, long lifespan, low maintenance, rapid response, and suitability for miniaturization [1–3].

TE materials generate an electric voltage in response to a temperature gradient and vice versa through the Seebeck and Peltier effects, respectively [3]. Various strategies have been developed to enhance the performance of TE materials, including minority charge carrier filtering, quantum confinement, and strengthening phonon scattering [4,5]. Metal oxide-based TE films provide a low-cost, efficient, and environmentally friendly platform for developing advanced TE materials comparable to conventional bulk single crystals [6]. These films are promising for applications in power generators, miniaturized electronics, and wearable sensors for the Internet of Things (IoT) [6,7].

Zinc oxide (ZnO), an n-type semiconducting metal oxide, is notable for its abundance, non-toxicity, broad operating temperature range, excellent oxidation resistance, and ease of processing [8,9]. These properties make ZnO a strong candidate to address the limitations of conventional TE materials such as Bi_2Te_3, PbTe, SnO_2, and SiGe [6,8]. ZnO's high lattice thermal conductivity can be reduced through nanostructuring, enhancing its TE performance by refining grain size and increasing phonon scattering at grain boundaries [10].

Doping ZnO with suitable elements further optimizes charge transport and improves its TE properties [11–13]. Among various dopants, Gallium (Ga) is the most efficient for ZnO due to its unique properties, including low reactivity, high oxidation resistance, and minimal lattice distortion [11]. Ga doping improves stress relaxation and enhances electrical conductivity, while its surfactant effect results in smoother film surfaces [11]. Ga^{3+} ions, with an ionic radius of 0.62 Å, closely match the ionic radius of Zn^{2+} (0.60 Å), allowing for easy substitution in the ZnO lattice without significantly distorting the crystal structure [14]. The stability of the Ga/Zn solid solution also reduces the possibility of impurity formation, making Ga an ideal dopant for improving the thermoelectric performance of ZnO films [14]. There has been considerable interest recently in developing ZnO films either constrained by a substrate or as free-standing [15].

Substrate-constrained ZnO films are often fabricated using physical vapor deposition (PVD) and chemical vapor deposition (CVD) methods [16–18]. Sputtering, a widely used PVD method, has been demonstrated as an effective technique for fabricating ZnO thin films, as reported by Murmu et al. [19]. However, these deposition methods often require harsh processing conditions, which can limit material compatibility and substrate options [20]. Alternatively, Munaga et al. introduced a simpler, low-cost chemical solution deposition (CSD) method to develop uniform TE films on glass substrates using spin-coating [21]. Nonetheless, substrate properties can constrain the mechanical and thermoelectric properties of ZnO films [21]. For instance, Diestel et al. found that the high heat capacity of the substrate, compared to the film, reduces the useable temperature differential, thereby lowering the efficiency [22]. Furthermore, Alvarez-Quintana et al. demonstrated that substrate properties, including the film-to-substrate thickness ratio, significantly affect the thermoelectric efficiency of bismuth (Bi) films [23]. Simunkova et al. also emphasized the importance of adhesive and cohesive behavior on the mechanical properties of the film-on-substrate system [24].

Developing free-standing TE films, which eliminate substrate-induced constraints, is desirable for improving TE performance and achieving flexibility in applications such as wearable devices [25]. Additive manufacturing, particularly 3D printing, has emerged as a promising method for producing free-standing TE films. This technique enables the rapid, cost-effective, and reproducible fabrication of films with complex designs based on computer-aided design (CAD) models [26]. By removing substrate constraints, 3D printing can
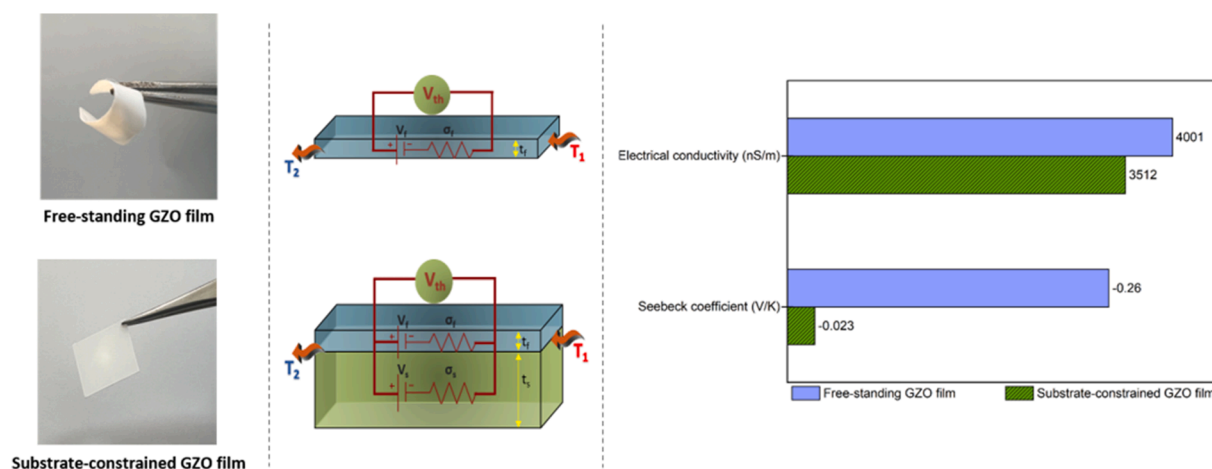

Fig. 1. Schematic of the experimental processes for developing free-standing and substrate-constrained GZO films.

overcome the scalability and design challenges associated with conventional film-on-substrate processes [27,28]. For example, Zhang et al. developed 3D-printed TE films based on bismuth telluride (Bi_2Te_3) with enhanced TE properties [28]. However, tellurium (Te)-based compounds are limited by their brittleness, toxicity, and scarcity, making them less suitable for widespread application [6, 28]. Therefore, developing alternative TE films based on earth-abundant, non-toxic materials like ZnO is critical for advancing TE technologies [6]. Additive manufacturing of such TE films will also enhance the development of next-generation TE modules with better sustainability and performance, enabling novel applications [29].

The structure and thermoelectric behavior of TE films could be influenced by the presence or absence of a substrate, which has not yet been thoroughly investigated for TE films based on earth-abundant and safe elements. In the present work, free-standing and substrate-constrained Ga-doped ZnO (GZO) films will be developed from different formulated inks and processing routes, as shown in Fig. 1. 3D printing will be used to produce substrate-free GZO films from an ink of photocurable resin and GZO nanoparticle additives. Substrate-constrained GZO films will be deposited through spin-coating a formulated ink of GZO nanoparticles with a polymer binder and volatile solvents onto a soda lime glass substrate, followed by post-treatment with annealing to burn out the binder and consolidate the film. This work will experimentally analyze the structural, chemical, and thermoelectric properties of the developed free-standing and substrate-constrained GZO films using various characterization techniques, including XRD, FE-STEM, XPS, C-AFM, and TE measurements.

2. Experimental

2.1. Materials

GZO nanopowder was supplied by Nanochemazone with 99 % purity and an average particle size of 50–60 nm. Photocurable LCD-C resin was provided by SparkMaker, with a liquid density of 1.10 g/cm^3 and UV curing in the range of 355–420 nm. Polyethylene oxide (PEO) powder, with a molecular weight of 600,000–1,000,000 g/mol, was obtained from Acros Organics. All materials were utilized as received without further purification.

2.2. Methods

2.2.1. Free-standing GZO films

GZO nanopowder was added to the photocurable LCD-C resin in equivalent weight fractions and homogenized through overnight magnetic stirring. Prolonged stirring times have been employed in the literature to ensure thorough dispersion of nanoparticles and to prevent the formation of agglomerates, which can negatively affect both the structural integrity and thermoelectric performance of the films [30–32]. CHITUBOX software was used to slice a 3D CAD model for printing, with parameters set at a 120-s exposure time and a lift speed of 60 mm/min. A Phrozen Sonic Mini Resin 3D Printer, operating at a 405 nm photocuring wavelength, printed a 50 μm layer of the photocurable resin-GZO nanocomposite, as demonstrated in Fig. 1. Free-standing GZO films were immersed in isopropyl alcohol to remove uncured resin and then dried at room temperature for a clean, smooth surface finish.

2.2.2. Substrate-constrained GZO films

GZO nanopowder was mixed with a PEO binder dissolved in a 1:1 (v/v) ratio of distilled water (dH$_2$O) and ethanol (EtOH) to achieve a GZO concentration of 1.24 M [33]. The resulting GZO/PEO ink underwent 30 min of ultrasonication followed by overnight magnetic stirring to ensure homogenization. Soda-lime glass (SLG) slides having 1.1 mm thickness, used as substrates, were ultra-sonically cleaned for 10mins in a mixture of Acetone, dH$_2$O, and Hellmanex III, followed by Methanol and Isopropyl Alcohol, consecutively to remove contaminants and then dried in an oven at 80 °C for 15min to enhance the wettability. The GZO/PEO ink was deposited onto the pre-cleaned SLG substrates using a micropipette with a 500 μL volume and spin-coated at 3000 rpm for 60 s with an Ossila spin coater (L2001A3-E461, UK). Substrate-constrained GZO films were then annealed in an inert argon (Ar) atmosphere using a tube furnace (SYN-1200CFTB, Henan Synthe, China) at a uniform temperature of 200 °C, with a constant heating/cooling rate of 10 °C/min and a dwell time of 30 min, as shown in Fig. 1. The annealing temperature of 200 °C was maintained to facilitate the removal of the low-content insulating PEO binder and to promote adequate connectivity among the GZO nanoparticles, consolidating the film with minimal structural deformation [33].

2.3. Characterizations

2.3.1. Structure and morphology

Phase identification and grain size of the free-standing and substrate-constrained GZO films were determined using an X-ray diffractometer (XRD; PANalytical EMPYREAN, UK) equipped with a Cu/Kα radiation source (λ = 1.54 Å). Microstructural features and elemental distribution of the GZO films were investigated via analytical field emission scanning transmission electron microscopy (FE-STEM; Thermo Fisher Scientific Talos F200X, USA) in conjunction with energy dispersive X-ray spectroscopy (EDS). TEM samples were prepared as TEM lamellae using focused ion beam scanning electron microscopy (FIB/SEM; Thermo Fisher Scientific Versa 3D Dual Beam, USA). The chemical state and elemental composition of the GZO films were analyzed using X-ray photoelectron spectroscopy (XPS; Kratos AXIS Ultra DLD, USA). Surface topography and electrical characteristics of the GZO films were examined using conductive atomic force microscopy (C-AFM; Asylum Research MFP-3D, USA) with an ORCA probe.

2.3.2. Thermoelectric properties

The electrical conductivity and Seebeck coefficient of free-standing and substrate-constrained GZO films were measured at room temperature using the experimental setup developed by Hasan et al. [34]. The setup consisted of an infrared thermometer (RayTemp 8, UK), hot plate, and source measure unit (SMU; Keithley 2400, USA). Electrodes were created on both ends of the free-standing GZO film using conductive silver paste (Sigma-Aldrich). An interdigitated ITO substrate (S162) served as the electrodes for substrate-constrained GZO film. The SMU instrument was used to measure resistance and evaluate the electrical conductivity of the films. To determine the Seebeck coefficient, a hot plate was used to heat one side of the film and create a temperature gradient (ΔT), generating a thermoelectric voltage (ΔV) measured with the SMU instrument. The slope technique was then used to determine the Seebeck coefficient ($S = \Delta V / \Delta T$) values from the generated thermoelectric voltage as a function of the temperature gradient on free-standing and substrate-constrained GZO films.

3. Results and discussions

3.1. Structure and morphology

#### 3.1.1. Crystallinity and crystallographic characteristics

The crystallinity, microstructure features, and surface morphology of free-standing and substrate-constrained GZO films were analyzed using XRD, FE-STEM, XPS, and AFM. Fig. 2(a) shows the XRD patterns of polycrystalline GZO films developed from substrate-free and substrate-constrained models, featuring sharp and narrow peaks that coincide with the standard ZnO hexagonal wurtzite structure peaks (JCPDS: 36–1451) [35]. This good agreement in peak positions and intensities for GZO films confirms their phase purity and uniform crystal structure. Fig. 2(b) illustrates the standard hexagonal wurtzite structure of GZO, depicting atomic configurations in indexed crystallographic planes such as (010), (002), and (101). These characteristic peaks are prominently observed with strong intensities at low Bragg angles (2θ) of 31.8°, 34.4°, and 36.3° in the XRD profiles of GZO films. Additional low-intensity diffraction peaks, marked with asterisks at 18.8°, 43.8°, and 58.9°, are observed in the XRD pattern of the substrate-constrained GZO film. These peaks may be attributed to reflections from the substrate, indicating potential interactions between the film and the substrate [29].

The texture coefficient (TC) for a specific crystallographic plane (hkl) represents the degree of texture on that plane, with any deviation from the standard reference indicating a preferred growth orientation [36]. It is quantified as follows [37]:

$$TC(hkl) = \frac{I(hkl)/I_o(hkl)}{N^{-1}\sum\limits_{n} I(hkl)/I_o(hkl)} \tag{1}$$

Where $I(hkl)$ is the measured XRD intensity of the film, $I_o(hkl)$ is the standard reference intensity, N is the number of reflections, and n is the number of diffraction peaks [37]. Table 1 presents the calculated TC values for the most intense peaks in the XRD patterns of GZO films. The (101) plane exhibits the highest TC, indicating a preferential orientation of GZO grains. This orientation correlates with the increased intensity of the (101) peak compared to the (010) and (002) peaks in the XRD patterns of GZO films. The processing route plays a key role in determining the degree of texture in polycrystalline films, contributing to the films' properties in line with the processing-microstructure-texture-property relationship [38].

Kennedy et al. demonstrated that the preferred orientation of ZnO films on SiO₂/Si substrates, prepared by ion beam sputtering, can be adjusted based on annealing conditions [39]. For instance, vacuum-annealed films exhibited (100) orientation, while air-annealed films showed (002) orientation [39]. Several factors influence preferential growth in polycrystalline films, including surface free energy, nucleation dynamics, surface diffusion, grain growth conditions, post-growth treatments, and film-substrate interactions [40]. Hu et al. reported that textured ZnO films with preferential (101)-oriented grains exhibit excellent light-trapping effects and electrical
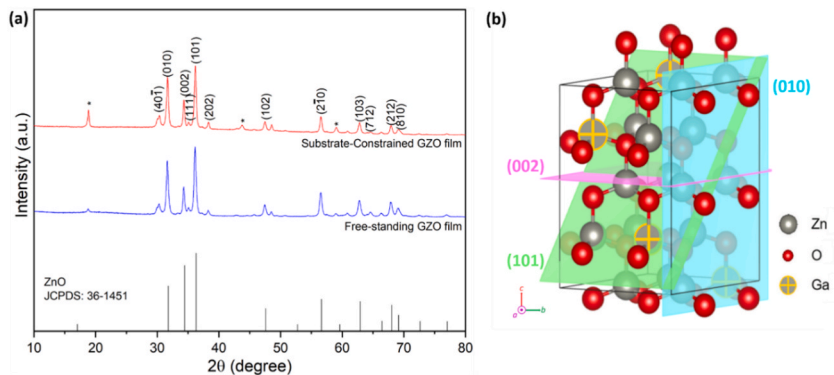
Fig. 2. (a) XRD patterns of free-standing and substrate-constrained GZO films. (b) Crystal structure of GZO with atomic configurations in the intense (010), (002), and (101) planes.

Table 1

XRD analysis of free-standing and substrate-constrained GZO films, showing the calculated texture coefficient (TC), crystallite size (D), microscopic lattice strain (ε), lattice parameters (a and c), unit cell volume (V), Zn–O bond length (L), density (ρ), out-of-plane strain (ε_{zz}), and in-plane stress (σ).

Sample	TC (hkl)			D (nm)	ε (%)	Lattice parameters				ρ (g/cm^3)	ε_{zz} (%)	σ (GPa)
	(010)	(002)	(101)			a (Å)	c (Å)	V (Å^3)	L (Å)			
Free-standing GZO film	1.42	1.23	1.89	22.2	0.341	3.25	5.21	47.6	1.98	5.68	0.032	−0.075
Substrate-constrained GZO film	1.51	1.20	1.84	24.8	0.089	3.26	5.23	48.1	1.99	5.62	0.442	−1.030

properties, making them suitable for transparent conducting electrodes [41].

The contribution of crystallite size (D) and microscopic lattice strain (ε) to the diffraction peak broadening profile in the XRD patterns of GZO films can be quantified using the Warren-Averbach method as follows [42]:

$$\frac{\beta_{hkl}^2}{\tan^2 \theta} = \frac{l}{D}\left(\frac{\beta_{hkl}}{\tan \theta \sin \theta}\right) + 25\left(\varepsilon^2\right)$$

(2)

Where β_{hkl} is the width of the (hkl) peak at half-maximum intensity in radians, λ is the wavelength of the X-ray beam, θ is the diffraction angle of the peak position in radians, D is the average grain size, and ε is the lattice strain [42]. Both GZO films exhibit a nanocrystalline structure, with the free-standing GZO film featuring finer crystallites (22 nm), as shown in Table 1. This finer structure might be attributed to the reduced clustering of GZO nanoparticles, hindered by interactions with polymeric chains from the photocurable resin matrix [43]. These interactions could also improve the dispersion of GZO nanoparticles, enhancing the interphase properties in free-standing GZO films [44]. The higher lattice strain in the free-standing GZO film (0.341 %) may be due to localized structural distortions at the interfaces between GZO nanoparticles and the resin matrix [18]. Lou et al. proposed that engineering the lattice strain can significantly reduce lattice thermal conductivity, thereby enhancing the thermoelectric performance in polycrystalline films [45].

The microstructure data of ZnO films, including lattice constants (a, b, and c), can be calculated using the crystallographic plane indices (h, k, and l) as follows [46]:

$$d_{(hkl)} = \left[\frac{4}{3}\left(\frac{h^2 + k^2 + hk}{a^2}\right)\right]_0^{-0.5}$$

(3)

Where $d_{(hkl)}$ is the inter-planar spacing derived from Bragg's law and XRD patterns [46]. The lattice parameters of the standard reference ZnO are $a_o = b_o = 3.25$ Å and $c_o = 5.21$ Å [41]. Table 1 shows that the substrate-constrained film exhibits higher lattice constants than the reference, which could be attributed to Ga doping, substrate interactions, or variations in synthesis parameters [47]. Ennaceri et al. reported that ZnO films with a higher c-lattice constant than strain-free ZnO bulk are subjected to tensile strain along the c-axis, perpendicular to the film's substrate surface [48].

The average uniform strain (ε_{zz}) in the lattice along the c-axis can be estimated from the lattice parameters using the following equation [49]:

$$\varepsilon_{zz} = \frac{c - c_o}{c_o} * 100\%$$

(4)

The developed GZO films, as shown in Table 1, exhibit positive values for ε_{zz}, indicating the presence of tensile strain along the c-axis, with a more pronounced effect in the substrate-constrained film, which correlates with the increase in its c-lattice constant. For the substrate-free GZO film, ε_{zz} is negligible, confirming the effective relaxation of its crystal structure. This relaxation may minimize surface energy and enhance the film's stability [50].

As a result of out-of-plane tensile strains, the unit cell may elongate along the c-axis, leading to changes in the volume (V) of the unit cell and the bond length (L) of Zn–O in the developed films. These changes can be calculated using the following relations [49,50]:

$$V = \frac{\sqrt{3}}{2}a^2 c$$

(5)

$$L = \sqrt{\left(\frac{a^2}{3} + \left(\frac{1}{2} - u\right)^2 c^2\right)}$$

(6)

where u is the internal parameter of the wurtzite-structured ZnO, estimated as follows [50]:

$$u = \left(\frac{1}{3}\right)\left(\frac{a^2}{c^2}\right) + \frac{1}{4}$$

(7)

Table 1 shows that the substrate-constrained GZO film exhibits a higher unit cell volume of 48.1 Å^3 and bond length of 1.99 Å compared to the standard values of 47.5 Å^3 and 1.98 Å, respectively [41]. Malek et al. correlated the increase in the a and c lattice parameters to a decreased electrostatic attraction between Zn^{2+} and O^{2-} ions in ZnO films deposited on glass substrates via the dip-coating technique [49]. A reduced electrostatic attraction between the zinc and oxygen ions results in inferior electrical transport,

as the atoms are more distant due to the longer Zn–O bonds [51]. This may also weaken the Zn–O bond, reduce the dissociation energy required to break it, and subsequently lower the thermal stability of the GZO film [51].

The tensile strain along the c-axis may also induce a compressive force in the plane of the deposited film, leading to increased compressive stress in the lateral direction [52]. The stress in the plane (σ) of GZO films can be determined using the following biaxial stress model expression [52]:

$$\sigma = \frac{2C_{13}^2 - C_{33}(C_{11} + C_{12})}{2C_{13}} *\varepsilon_{zz} \tag{8}$$

where C_{ij} are the bulk ZnO elastic stiffness constants: C_{11} = 208.8 GPa, C_{12} = 119.7 GPa, C_{13} = 104.2 GPa, and C_{33} = 213.8 GPa [49]. This equation gives the following numerical stress relationship:

$$\sigma = -233 GPa *\varepsilon_{zz} \tag{9}$$

The negative sign of σ values in Table 1 indicates that the developed GZO films are under compressive stress. The substrate-free film shows minimal stress, with a magnitude of −0.075 GPa, approaching that of unstressed bulk ZnO, while the substrate-constrained film exhibits significant compressive stress, reaching −1.03 GPa. The total residual stress in the film typically consists of extrinsic and intrinsic stresses [49]. In the substrate-constrained model, the residual stress in the GZO film is mainly due to extrinsic factors, such as mismatches in lattice parameters and thermal expansion coefficients between the film and substrate [49]. In contrast, intrinsic stresses dominate the substrate-free GZO film, resulting in microstructural lattice strain, as evidenced by the high strain values in Table 1 [51]. Tuan Thanh Pham et al. observed that residual stresses significantly impact the thermoelectric performance of GZO films, with higher power factors found in films with lower compressive stress [51].

The theoretical density (ρ) of the developed films can also be estimated from the lattice constants as follows [48]:

$$\rho = \frac{1.6609 *MW *n}{a^2 c \sqrt{\frac{3}{4}}} \tag{10}$$

where *MW* is the molecular weight of ZnO (81.41 g/mol), and *n* is the number of molecules per unit cell, which equals 2 [48]. The calculated density values in Table 1 show that the free-standing GZO film is close to 5.69 g/cm^3, similar to bulk ZnO, while the substrate-constrained film has a lower density of 5.62 g/cm^3. Saini et al. linked the decrease in density of ZnO films to a high degree of porosity, which degrades thermoelectric performance by causing film discontinuity, hindering intergranular electron transport, and reducing electrical conductivity [53].

3.1.2. Nanostructure features and elemental distribution

The high-resolution bright-field STEM micrographs in Fig. 3 (a) and (b) offer insights into the nanostructure of substrate-constrained and free-standing GZO films. These images reveal randomly oriented GZO nanoparticles forming interconnected
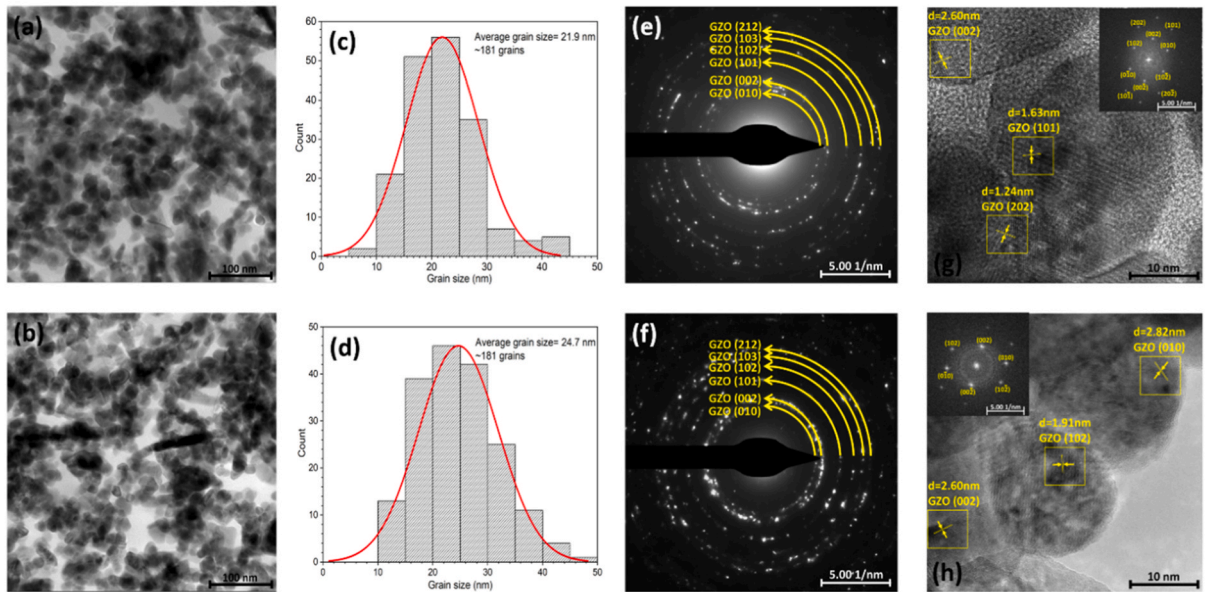
Fig. 3. High-resolution FE-STEM analysis of free-standing (top row) and substrate-constrained (bottom row) GZO films, featuring: (a–b) Bright-field STEM images, (c–d) Grain size distribution, (e–f) Diffraction patterns, and (g–h) HR-STEM images with upper insets showing FFT patterns.

networks through heterogeneous grain boundaries at various angles. Notably, the substrate-constrained film displays discontinuities attributed to pores formed during annealing, which removes the insulating binder, while the free-standing film exhibits additional interfaces with the photocurable resin matrix during the photopolymerization process. Grain size distribution profiles obtained from BF-STEM images (Fig. 3(c) and (d)) indicate average sizes of 21.9 nm and 24.7 nm for free-standing and substrate-constrained films, respectively, consistent with XRD analysis. Additionally, the diffraction patterns (Fig. 3(e) and (f)) reveal polycrystalline structures for both films, with equiaxed grains in circular rings and random orientations, corresponding to various crystallographic planes observed in XRD patterns.

In Fig. 3 (h), the HR-STEM micrograph of the substrate-constrained GZO film illustrates interactions among randomly oriented GZO nanoparticles, suggesting improved connectivity post-annealing. This enhancement may increase film conductivity and potentially induce structural disorder at grain boundaries, thereby increasing the film's Seebeck coefficient [44]. Similarly, Fig. 3 (g) shows interactions among randomly oriented GZO nanoparticles and interfaces with the resin matrix in the free-standing GZO film, potentially enhancing the film's energy filtering effect and Seebeck coefficient. Fig. 3 (g) and (h) also depict the interplanar spacings of the GZO nanoparticles corresponding to specific XRD diffraction planes. The upper insets in Fig. 3 (g) and (h) present the fast Fourier transform (FFT) patterns of the HR-STEM micrographs, confirming a hexagonal structure consistent with the standard ZnO lattice. This observation aligns with the crystallinity findings from the sharp and narrow XRD diffraction patterns. Fig. 4 (a) and (b) showcase high-angle annular dark-field scanning transmission electron microscopy (HAADF-STEM) images of both films, along with corresponding EDS elemental mapping images. These images reveal a uniform distribution of Ga, Zn, and O elements on the SLG substrate (Si) and within the resin matrix (C), suggesting potential enhancements in the films' thermoelectric properties [54].

3.1.3. Chemical state and elemental composition

XPS analysis examined the chemical composition and binding states of both substrate-constrained and free-standing GZO films. Fig. 5 presents the full survey XPS spectra, highlighting the core levels of C 1s, O 1s, Zn 2p, and Ga 2p at various binding energies. These peaks correspond to GZO nanoparticles, the resin matrix in free-standing films, or the polymeric binder in substrate-constrained films. The higher intensity of the C 1s core level in the free-standing film is attributed to the presence of the resin matrix, emphasizing the compositional differences between the two films. The increased intensity of the Zn 2p peak relative to the Ga 2p peak confirms the successful doping of Ga into the ZnO lattice.

Gaussian spectral fitting of the XPS data provides further insights into the binding states of the elements. Fig. 6 (a) and (b) decompose the C 1s peak into C–O–C and H–C/C–C peaks, indicating the presence of a resin matrix in the free-standing film and binder residues in the substrate-constrained film. Fig. 6 (c) and (d) fit the Ga 2p core level peaks, revealing Ga–O bonds and Ga $2p_{3/2}$ spin-orbit peaks with slight variations. This shift in peak positions suggests different chemical environments and substrate interactions, leading to high in-plane stresses, as observed from the XRD analysis [55]. The binding energy of the Ga 2p peaks typically occurs around 1115.1 eV and 1114.7 eV for the free-standing and substrate-constrained GZO films, respectively, further confirming the incorporation of Ga into the ZnO lattice, consistent with the literature [55].

Similarly, Fig. 6 (e) and (f) show the Zn 2p core level spectra, attributed to Zn–O–Ga bonds and the spin-orbit splitting of Zn $2p_{1/2}$ and Zn $2p_{3/2}$, confirming the presence of Ga-doped ZnO nanoparticles in both films. The binding energies for the Zn 2p peaks are generally observed around 1017.9 eV (Zn $2p_{3/2}$) and 1040.8 eV (Zn $2p_{1/2}$), which confirms the oxidized state of Zn and supports the stability of the GZO films. Fig. 6 (g) and (h) display the O 1s spectra peaks, confirming the presence of heterogeneous interfacial bonds and interdiffusion regions between the resin matrix and GZO nanoparticles in the free-standing film. These findings align with TEM and XRD analyses, indicating distinct chemical environments within the GZO films, which may influence their thermoelectric properties [21]. The O 1s peak intensities suggest that the Zn–O bond is dominant in the substrate-constrained film, implying low-density
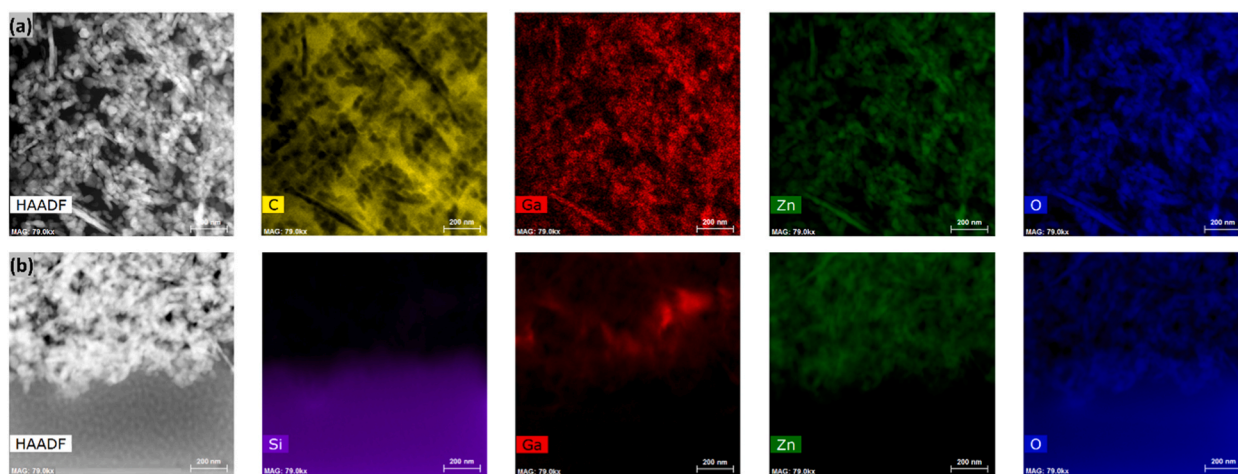
Fig. 4. HAADF-STEM images with corresponding EDS elemental mapping of C, Si, Ga, Zn, and O elements in (a) free-standing and (b) substrate-constrained GZO films.
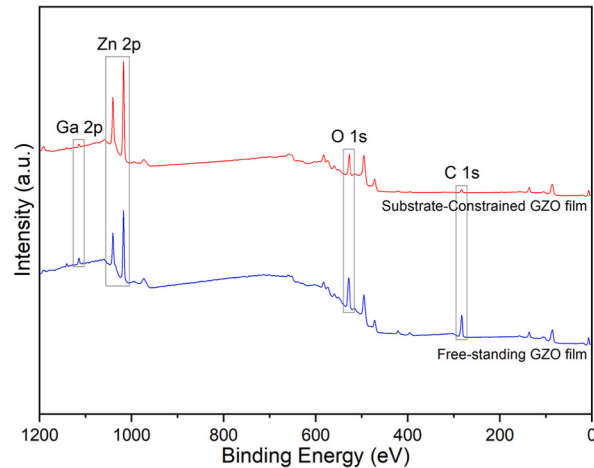
Fig. 5. Full survey XPS spectra of free-standing and substrate-constrained GZO films.
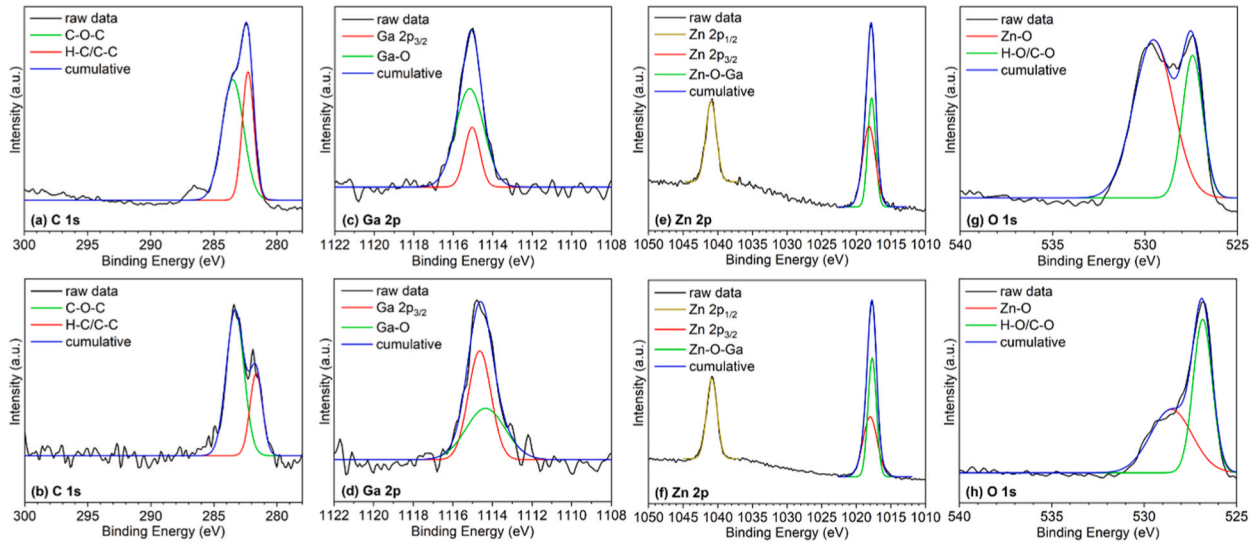
Fig. 6. XPS spectra of (a–b) C 1s, (c–d) Ga 2p, (e–f) Zn 2p, and (g–h) O 1s core levels for free-standing (top row) and substrate-constrained (bottom row) GZO films.

heterogeneous interfaces due to minimal binder residues following annealing.

Table 2 presents the elemental compositions of both substrate-constrained and free-standing GZO films, confirming the presence of the Ga dopant, which indicates the formation of n-type Ga-doped ZnO films. Variations in ink formulations and processing techniques result in differences in GZO film compositions, significantly affecting their properties [56]. In the free-standing film, the Zn and C contents are nearly equal. In contrast, Zn predominates over C in the substrate-constrained film, primarily due to the removal of binder material during annealing, leaving 6 wt% of residual binder. Table 2 also shows a higher Zn ratio in the substrate-constrained GZO film compared to the free-standing GZO film. This significant difference in Zn and O ratios can be attributed to several factors related to the manufacturing processes and material interactions. Higher temperatures and varying oxygen partial pressures during post-deposition annealing may enhance Zn incorporation in substrate-constrained films [57]. Additionally, substrate-induced stresses could affect

Table 2
XPS analysis of the elemental composition in free-standing and substrate-constrained GZO films.

| Sample	Element (wt%)			
	Ga	Zn	O	C
Free-standing GZO film	2.46	38.4	26.0	33.1
Substrate-constrained GZO film	1.20	75.2	17.7	5.90

oxygen diffusion and film growth kinetics, promoting Zn adsorption and leading to oxygen vacancies [58]. Raidou et al. found that the substrate's nature influences the crystal structure and morphology of ZnO films, resulting in distinct XPS behaviors [58]. In contrast, free-standing films developed through 3D printing exhibit a more balanced incorporation of Zn and O, as they are not subject to substrate or post-deposition annealing constraints.

3.1.4. Surface topography and electrical characteristics

Fig. 7 presents the C-AFM surface topography and current mapping images for free-standing and substrate-constrained GZO films. In Fig. 7(a) and (b), the AFM topography images reveal a fine granular structure for the developed GZO films, consistent with nanostructural observations from XRD and TEM analyses. The interactions between GZO nanoparticles exhibit better interconnectivity in the free-standing GZO film, resulting in a surface roughness of 262 nm, compared to 148 nm for the substrate-constrained film. This difference is attributed to the dense structure formed from multiple nano-sized GZO particles dispersed homogeneously in the photocurable resin matrix, as observed in TEM and XPS analyses. This structure potentially enhances interfacial bonds and thermoelectric properties [42]. The development of a dense structure in the free-standing GZO film is also corroborated by TEM analysis, which shows a bulk-like calculated density based on XRD analysis. Mousavi et al. reported that increased surface roughness decreases lattice thermal conductivity due to enhanced phonon-surface roughness scattering [59]. Similarly, Baghdadi et al. demonstrated that modifying the surface roughness of ZnO nanomaterials can improve thermoelectric properties by promoting significant phonon scattering in all directions [60].

In Fig. 7(c) and (d), the current mapping images and line profiles illustrate conductivity domains of 200 pA and 175 pA for free-standing and substrate-constrained GZO films, respectively. The conductive domain is recognized by high carrier delocalization, possibly due to the crystalline structure of the developed films, as revealed by XRD profiles, which enhances the mobility of charge carriers [61]. However, the current profile of the substrate-constrained GZO film reveals a non-uniform conductivity domain across the film compared to the more uniform free-standing model. The potential interactions between the film and substrate in the substrate-constrained model may contribute to this non-uniformity, potentially leading to anisotropic electrical conductivity that varies depending on the location within the substrate-constrained GZO film [62]. The inhomogeneous conductivity domain may also be correlated with the evolution of a porous microstructure in the substrate-constrained GZO film, as observed in TEM analysis. These pores could disrupt the connectivity of GZO nanoparticles, impede electron transport, and hinder uniform current distribution throughout the film [63].
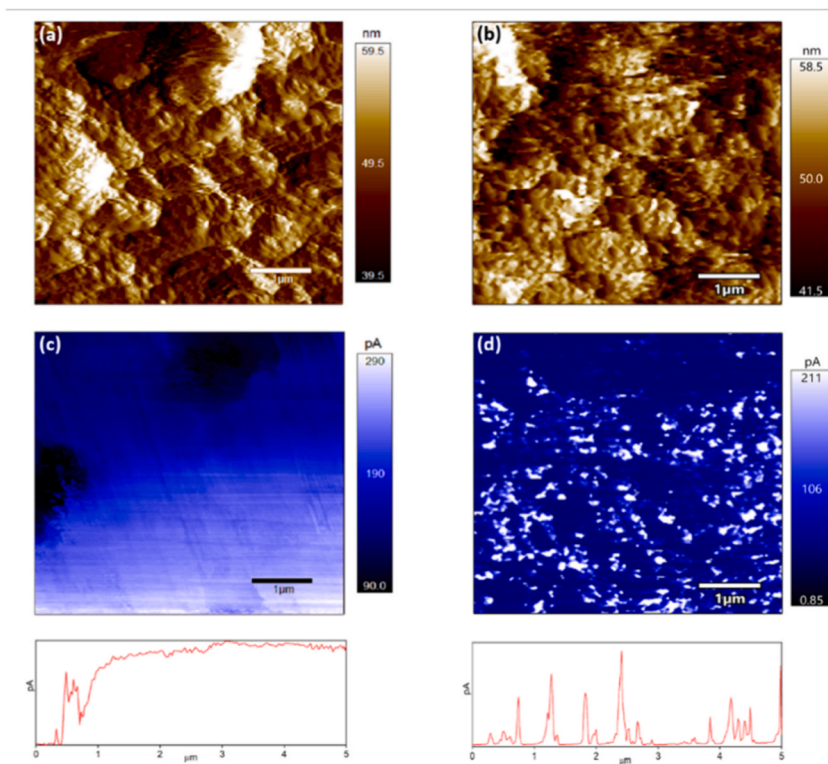
Fig. 7. C-AFM surface topography (a–b) and current mapping images (c–d) for free-standing (left-column) and substrate-constrained (right-column) GZO films. All measurements were obtained from a $5 \times 5 \mu m^2$ surface area at a bias voltage of 10V.

3.2. Thermoelectric properties

The analysis of thermoelectric properties in both substrate-constrained and free-standing GZO films can differ significantly due to variations in heat flow paths [22]. In substrate-constrained films, heat flows along two parallel paths—through the substrate and the film—while in free-standing films, heat flows only through the film due to the absence of a substrate, as shown in Fig. 8(a) and (b). In film-substrate systems, part of the heat current may dissipate into the substrate, potentially creating a thermal or electrical shunt for the thermoelectric film, depending on the electrical and thermal characteristics of the substrate [42]. Considering the electrical current flowing through parallel paths, the thermoelectric voltage (V_{th}) depends on the electrical conductivities of both the substrate (σ_s) and the film (σ_f), as well as the thickness of the film (t_f) and the substrate (t_s), thereby affecting the system's thermoelectric performance [23]. Alvarez-Quintana et al. noted that when heat flows cross-plane in the substrate-film system, the heat distribution in each material is similar [23]. Consequently, an increase in the substrate's temperature reduces the total temperature rise in the film, thereby affecting its thermoelectric performance [24].

The free-standing GZO film demonstrates a 14 % enhancement in room-temperature electrical conductivity compared to the substrate-constrained GZO film, as shown in Fig. 8(c). This improvement is directly attributed to the low-stress crystalline structure and densely packed microstructure observed in the free-standing GZO film, as confirmed by XRD and TEM analyses. In contrast, the XRD analysis of the substrate-constrained film revealed significant lattice strain and compressive stress, which likely strengthen electron-lattice interactions, reduce mean free path of electrons, and increase electron scattering, thereby lowering the electrical conductivity [76]. These findings align with the decrease in calculated density from XRD analysis of the substrate-constrained GZO film, which correlates with the high porosity observed via TEM analysis, indicating a lack of continuity in the structure and contributing to reduced intergranular electron transport [77]. Additionally, film-substrate interactions may affect the electrical conductivity of the substrate-constrained GZO film, potentially creating a non-uniform conductivity domain, as identified via XPS and C-AFM analyses.

The Seebeck coefficient values for the developed GZO films are negative, indicating typical n-type conductivity behavior, where electrons are the major charge carriers [21]. Compared to the substrate-constrained film, the free-standing film exhibits a remarkable 91 % improvement in the room-temperature Seebeck coefficient, as shown in Fig. 8(c). This significant enhancement is attributed to nanostructure evolution in the free-standing film, which features refined grains and heterogeneous grain boundaries. These structures enhance the energy-filtering effect, selectively scattering low-energy electrons and increasing the magnitude of the Seebeck coefficient [78]. The thickness ratio between the substrate and the film, denoted as $X = t_s/t_f$, may also play a crucial role in inducing V_{th} in response to temperature differences across the film-substrate system [23]. TEM analysis revealed a thickness of 477 nm for the substrate-constrained GZO film compared to 1.1 mm for the SLG substrate. This results in a high thickness ratio of 2306, indicating substrate dominance, thereby behaving as a non-thermoelectric system. The challenges of substrate-constrained films in thermoelectric applications, especially at nanoscale thicknesses, emphasize the importance of utilizing free-standing films, which eliminate substrate interference [22].

Fig. 8(d) compares the room-temperature power factor (PF) of the developed GZO films with other thermoelectric films, calculated as follows [6]:

$$PF = \sigma * S^2 \tag{11}$$

where σ is the electrical conductivity, and S is the Seebeck coefficient [6]. According to the Mott relation, a decrease in electrical conductivity typically leads to an increase in the Seebeck coefficient, while the Wiedemann–Franz law correlates higher electrical conductivity with increased thermal conductivity [79]. These physical constraints limit thermoelectric efficiency, complicating the optimization of the power factor. The free-standing GZO nanocomposite film exhibits a PF of 261 nW/m·K^2 at room temperature, representing a 70 % increase compared to a MoS_2/CNT composite film (160 nW/m·K^2) on a PET substrate (via the doctor blade method), and an 89 % improvement compared to a ZnO film (60 nW/m·K^2) on a Kapton substrate (via the SILAR method) [66,70]. Furthermore, the PF demonstrates a 94 % enhancement over an Al-doped ZnO film (32 nW/m·K^2) on a quartz substrate (via thermal oxidation) and an 80 % improvement over the PVA-doped SWCNT flexible film (110 nW/m·K^2) produced via inkjet printing [64,68].

This clearly demonstrates the effectiveness of the proposed growth methodology in improving thermoelectric performance, driven primarily by the elimination of substrate constraints and the optimization of the crystalline microstructure through 3D printing technology. By removing the substrate, variations in structure and composition can influence localized stresses and enhance the thermoelectric properties of the developed GZO films [23]. Through 3D printing technology, tensile stresses in substrate-constrained films are effectively eliminated. While the PF of the developed GZO films still requires further improvement to exceed those achieved in high-performance GZO films using complex, high-cost deposition techniques, the proposed methodology enhances scalability, simplifies the fabrication process, and offers potential for further development using 3D printing technology [80–82]. These advancements could promote further utilization of this inexpensive, abundant, and environmentally friendly thermoelectric material in sustainable, tellurium-free thermoelectric devices [1,6].

4. Conclusions

This research investigated Ga-doped ZnO (GZO) films, composed of safe and abundant elements, comparing free-standing GZO films produced via 3D printing with substrate-constrained GZO films developed using conventional chemical methods. The study focused on analyzing their structural, chemical, and thermoelectric properties. XRD patterns revealed uniform crystal structures and
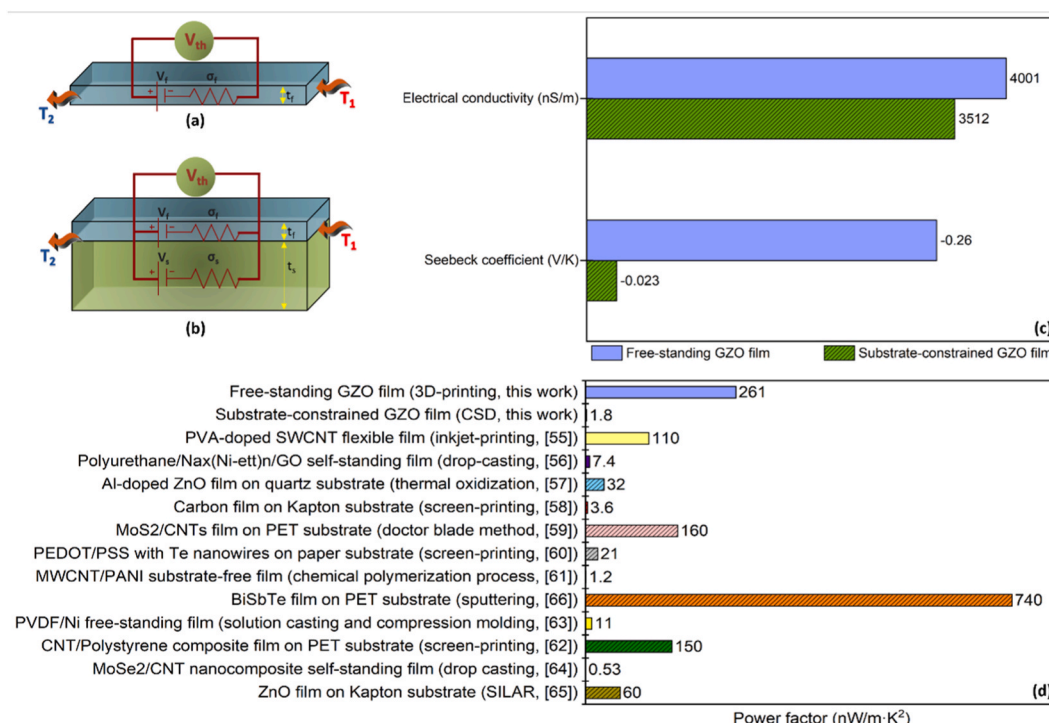
Fig. 8. Thermoelectric analysis of (a) free-standing and (b) substrate-constrained GZO films. (c–d) Room-temperature thermoelectric properties of GZO films in the present work compared to other thermoelectric films [64–75].

phase purity in both films; however, additional peaks in the substrate-constrained film suggested interactions with the substrate. FE-STEM micrographs showed granular nanostructures in both films, with the substrate-constrained film exhibiting discontinuities, likely due to annealing-induced pores. XPS analysis highlighted compositional differences, particularly in zinc and carbon content, resulting from the different fabrication methods. C-AFM analysis revealed variations in surface morphology and conductivity profiles, with the free-standing film demonstrating a more uniform conductivity domain. The free-standing GZO film exhibited superior electrical conductivity and a significantly enhanced Seebeck coefficient, leading to a higher power factor at room temperature. This study underscores the potential of 3D-printed, free-standing GZO films to advance thermoelectric applications by addressing the limitations of substrate-constrained films. Future research should explore performance at higher temperatures, examine thermal conductivity, and investigate the incorporation of multidimensional fillers to further enhance thermoelectric properties. These future directions will deepen the understanding of GZO films and pave the way for practical applications in sustainable energy harvesting.

CRediT authorship contribution statement

Aicha S. Lemine: Writing – original draft, Methodology, Investigation, Formal analysis, Data curation. **Jolly Bhadra:** Writing – review & editing, Supervision, Resources, Project administration. **Anton Popelka:** Software, Investigation, Formal analysis. **Muni Raj Maurya:** Software, Methodology, Formal analysis, Data curation. **Kishor Kumar Sadasivuni:** Visualization, Investigation, Formal analysis. **Rana Abdul Shakoor:** Software, Investigation, Formal analysis. **Ahmad Zubair:** Visualization, Software, Resources, Investigation, Conceptualization. **Noora J. Al-Thani:** Supervision, Resources, Funding acquisition, Conceptualization. **Anwarul Hasan:** Writing – review & editing, Supervision, Resources, Investigation, Conceptualization.

Data availability

Data will be made available upon request.

Declaration of Competing Interest

The authors declare that they have no known competing financial interests or personal relationships that could have appeared to influence the work reported in this paper.

Acknowledgments

References

[1] A. Ali, H. Shaukat, S. Bibi, W.A. Altabey, M. Noori, S.A. Kouritem, Recent progress in energy harvesting systems for wearable technology, Energy Strategy Rev. 49 (2023) 101124, https://doi.org/10.1016/j.esr.2023.101124.

[2] A.S. Lemine, O. Fayyaz, R.A. Shakoor, Z. Ahmad, J. Bhadra, N.J. Al-Thani, Effect of cold and hot compactions on corrosion behavior of p- and n-type bismuth telluride-based alloys developed through microwave sintering process, J. Alloys Compd. 939 (2023) 168763, https://doi.org/10.1016/j.jallcom.2023.168763.

[3] A.S. Lemine, F.M. El-Makaty, H.A. Al-Ghanim, K.M. Youssef, Experimental and modeling analysis of p-type Bi0.4Sb1.6Te3 and graphene nanocomposites, J. Mater. Res. Technol. 16 (2022) 1702–1712, https://doi.org/10.1016/j.jmrt.2021.12.096.

[4] J.V. Kennedy, P.P. Murmu, V. Karthik, Z. Liu, V. Jovic, T. Mori, W.L. Yang, K.E. Smith, Influence of carrier density and energy barrier scattering on a high Seebeck coefficient and power factor in transparent thermoelectric copper iodide, ACS Appl. Energy Mater. 3 (2020) 10037–10044, https://doi.org/10.1021/acsaem.0c01724.

[5] X. Chen, Z. Zhou, Y.H. Lin, C. Nan, Thermoelectric thin films: promising strategies and related mechanism on boosting energy conversion performance, J. Mater. 6 (2020) 494–512, https://doi.org/10.1016/j.jmat.2020.02.008.

[6] A.S. Lemine, J. Bhadra, N.J. Al-Thani, Z. Ahmad, Promising transparent and flexible thermoelectric modules based on p-type CuI thin films—a review, Energy Rep. 8 (2022) 11607–11637, https://doi.org/10.1016/j.egyr.2022.09.020.

[7] Y. Jia, Q. Jiang, H. Sun, P. Liu, D. Hu, Y. Pei, W. Liu, X. Crispin, S. Fabiano, Y. Ma, Y. Cao, Wearable thermoelectric materials and devices for self-powered electronic systems, Adv. Mater. 33 (2021) 1–46, https://doi.org/10.1002/adma.202102990.

[8] N. Vogel-Schäuble, Y.E. Romanyuk, S. Yoon, K.J. Saji, S. Populoh, S. Pokrant, M.H. Aguirre, A. Weidenkaff, Thermoelectric properties of nanostructured Al-substituted ZnO thin films, Thin Solid Films 520 (2012) 6869–6875, https://doi.org/10.1016/j.tsf.2012.07.046.

[9] I. Ullah, J. Jacob, F.F. Al-Harbi, K. Mahmood, A. Ali, M. Tamseel, S. Ikram, N. Amin, K. Javaid, L. Ben Farhat, S. Hussain, M. Yasir Ali, Investigating the potential of AgZnO thin film composites for waste heat recovery using Seebeck data, Opt. Mater. 127 (2022) 112318, https://doi.org/10.1016/j.optmat.2022.112318.

[10] P. Jood, R.J. Mehta, Y. Zhang, T. Borca-Tasciuc, S.X. Dou, D.J. Singh, G. Ramanath, Heavy element doping for enhancing thermoelectric properties of nanostructured zinc oxide, RSC Adv. 4 (2014) 6363–6368, https://doi.org/10.1039/c3ra46813e.

[11] Z. Zhou, M. Zou, Y. Xu, J. Lan, C. Liu, A. Ahmad, Y.H. Lin, C.W. Nan, High thermoelectric performance of high-mobility Ga-doped ZnO films via homogenous interface design, J. Am. Ceram. Soc. 104 (2021) 3992–3999, https://doi.org/10.1111/jace.17789.

[12] U. ur Rehman, K. ul Sahar, K. Mahmood, M. Kanwal, A. Ashfaq, M.F. Iqbal, H. Wang, N. Al-Zaqri, E. Hussain, A.A. Khan, Effect of Ni and Mn dopant on thermoelectric power generation performance of ZnO nanostructures synthesized via hydrothermal method, Mater. Chem. Phys. 304 (2023), https://doi.org/10.1016/j.matchemphys.2023.127907.

[13] U. ur Rehman, J. Jacob, F.F. Al-Harbi, A. Ashfaq, K. Mahmood, A. Ali, N. Amin, M. Amami, S. Hussain, K. Javaid, S. Ikram, K. ul Sahar, Modulation of thermoelectric power generation performance of ZnO nanostructures by controlling the Mn atoms concentration, Ceram. Int. 48 (2022) 16183–16187, https://doi.org/10.1016/j.ceramint.2022.02.165.

[14] Z.F. Zhou, G.K. Ren, X. Tan, R. Liu, C. Liu, Y.H. Lin, C.W. Nan, Enhancing the thermoelectric performance of ZnO epitaxial films by Ga doping and thermal tuning, J. Mater. Chem. A. 6 (2018) 24128–24135, https://doi.org/10.1039/c8ta06824k.

[15] A. Backen, S.R. Yeduru, M. Kohl, S. Baunack, A. Diestel, B. Holzapfel, L. Schultz, S. Fähler, Comparing properties of substrate-constrained and freestanding epitaxial Ni-Mn-Ga films, Acta Mater. 58 (2010) 3415–3421, https://doi.org/10.1016/j.actamat.2010.02.016.

[16] I. ul Haq, J. Jacob, K. Mehboob, K. Mahmood, A. Ali, N. Amin, S. Ikram, S. Hussain, Y. Feng, F. Ashraf, Effect of annealing temperature on the thermoelectric properties of ZnInO thin films grown by physical vapor deposition, Phys. B Condens. Matter 606 (2021) 412569, https://doi.org/10.1016/j.physb.2020.412569.

[17] S.D. Ponja, S. Sathasivam, I.P. Parkin, C.J. Carmalt, Highly conductive and transparent gallium doped zinc oxide thin films via chemical vapor deposition, Sci. Rep. 10 (2020) 1–7, https://doi.org/10.1038/s41598-020-57532-7.

[18] M. Tamseel, K. Mahmood, A. Ali, K. Javaid, H. Mufti, Controlled growth of Ag-ZnO thin films by thermal evaporation technique for optimized thermoelectric power generation, J. Alloys Compd. 938 (2023) 168507, https://doi.org/10.1016/j.jallcom.2022.168507.

[19] P.P. Murmu, J. Kennedy, B.J. Ruck, G.V.M. Williams, A. Markwitz, S. Rubanov, A.A. Suvorova, Effect of annealing on the structural, electrical and magnetic properties of Gd-implanted ZnO thin films, J. Mater. Sci. 47 (2012) 1119–1126, https://doi.org/10.1007/s10853-011-5883-z.

[20] A.T.T. Pham, H.K.T. Ta, Y. ren Liu, M. Aminzare, D.P. Wong, T.H. Nguyen, N.K. Pham, T.B.N. Le, T. Seetawan, H. Ju, S. Cho, K.H. Chen, V.C. Tran, T.B. Phan, Effect of annealing temperature on thermoelectric properties of Ga and in dually doped - ZnO thin films, J. Alloys Compd. 747 (2018) 156–165, https://doi.org/10.1016/j.jallcom.2018.02.349.

[21] V.V.P. Munaga, T. Krishnan, R.K. Borra, Structural, surface morphological, optical and thermoelectric properties of sol–gel spin coated Zn doped CdS thin films, SN Appl. Sci. 2 (2020) 1–12, https://doi.org/10.1007/s42452-020-2358-3.

[22] A. Diestel, R. Niemann, B. Schleicher, S. Schwabe, L. Schultz, S. Fähler, Field-temperature phase diagrams of freestanding and substrate-constrained epitaxial Ni-Mn-Ga-Co films for magnetocaloric applications, J. Appl. Phys. 118 (2015), https://doi.org/10.1063/1.4922358.

[23] J. Alvarez-Quintana, Impact of the substrate on the efficiency of thin film thermoelectric technology, Appl. Therm. Eng. 84 (2015) 206–210, https://doi.org/10.1016/j.applthermaleng.2015.03.062.

[24] S. Simunkova, O. Blahova, I. Stepanek, Mechanical properties of thin film-substrate systems, J. Mater. Process. Technol. 133 (2003) 189–194, https://doi.org/10.1016/S0924-0136(02)00231-5.

[25] M. Bharti, A. Singh, B.P. Singh, S.R. Dhakate, G. Saini, S. Bhattacharya, A.K. Debnath, K.P. Muthe, D.K. Aswal, Free-standing flexible multiwalled carbon nanotubes paper for wearable thermoelectric power generator, J. Power Sources 449 (2020) 227493, https://doi.org/10.1016/j.jpowsour.2019.227493.

[26] A.S. Lemine, J. Bhadra, K.K. Sadasivuni, A. Popelka, S. Yempally, Z. Ahmad, N.J. Al-Thani, A. Hasan, 3D printing flexible Ga-doped ZnO films for wearable energy harvesting: thermoelectric and piezoelectric nanogenerators, J. Mater. Sci. Mater. Electron. 35 (2024), https://doi.org/10.1007/s10854-024-13372-z.

[27] D. Park, S. Lee, J. Kim, Enhanced thermoelectric performance of UV-curable silver (I) selenide-based composite for energy harvesting, Sci. Rep. 11 (2021) 1–8, https://doi.org/10.1038/s41598-021-96267-x.

[28] X. Zhang, J. Chen, H. Zhang, P. Zhu, R. Wang, F. Li, B. Li, Enhanced thermoelectric performance of 3D-printed Bi2Te3-based materials via adding Te/Se, J. Mater. 9 (2023) 328–337, https://doi.org/10.1016/j.jmat.2022.10.002.

[29] Z.-F. Zhou, G.-K. Ren, X. Tan, R. Liu, C. Liu, Y.-H. Lin, C.-W. Nan, Enhancing the thermoelectric performance of ZnO epitaxial films by Ga doping and thermal tuning, J. Mater. Chem. A. 6 (2018) 24128–24135, https://doi.org/10.1039/C8TA06824K.

[30] A. Amin, R. Huang, D. Newbrook, V. Sethi, S. Yong, S. Beeby, I. Nandhakumar, Screen-printed bismuth telluride nanostructured composites for flexible thermoelectric applications, JPhys Energy 4 (2022), https://doi.org/10.1088/2515-7655/ac572e.

[31] A. Sahu, B. Russ, M. Liu, F. Yang, E.W. Zaia, M.P. Gordon, J.D. Forster, Y.Q. Zhang, M.C. Scott, K.A. Persson, N.E. Coates, R.A. Segalman, J.J. Urban, In-situ resonant band engineering of solution-processed semiconductors generates high performance n-type thermoelectric nano-inks, Nat. Commun. 11 (2020), https://doi.org/10.1038/s41467-020-15933-2.

[32] E. Jang, P. Banerjee, J. Huang, R. Holley, J.T. Gaskins, M.S. Bin Hoque, P.E. Hopkins, D. Madan, Thermoelectric performance enhancement of naturally occurring bi and chitosan composite films using energy efficient method, Electron 9 (2020) 1–12, https://doi.org/10.3390/electronics9030532.

[33] A.S. Lemine, J. Bhadra, A. Popelka, R.A. Shakoor, Z. Ahmad, N.J. Al-thani, A. Hasan, Synergistic effect of concentration and annealing on structural , mechanical , and room-temperature thermoelectric properties of n-type Ga-doped ZnO films, Ceram. Int. (2024), https://doi.org/10.1016/j.ceramint.2024.09.118.

[34] M.N. Hasan, M.I. Ahmad Asri, T. Saleh, A.G.A. Muthalif, M.S. Mohamed Ali, Wearable thermoelectric generator with vertically aligned PEDOT:PSS and carbon nanotubes thermoelements for energy harvesting, Int. J. Energy Res. 46 (2022) 15824–15836, https://doi.org/10.1002/er.8283.

[35] M.S. Sorayani Bafqi, A.H. Sadeghi, M. Latifi, R. Bagherzadeh, Design and fabrication of a piezoelectric out-put evaluation system for sensitivity measurements of fibrous sensors and actuators, J. Ind. Text. 50 (2021) 1643–1659, https://doi.org/10.1177/1528083719867443.

[36] C.Y. Tsay, C.W. Wu, C.M. Lei, F.S. Chen, C.K. Lin, Microstructural and optical properties of Ga-doped ZnO semiconductor thin films prepared by sol-gel process, Thin Solid Films 519 (2010) 1516–1520, https://doi.org/10.1016/j.tsf.2010.08.170.

[37] L. Znaidi, T. Touam, D. Vrel, N. Souded, S. Ben Yahia, O. Brinza, A. Fischer, A. Boudrioua, AZO thin films by sol-gel process for integrated optics, Coatings 3 (2013) 126–139, https://doi.org/10.3390/coatings3030126.

[38] C. V Thompson, Structure evolution during processing of polycrystalline films, Mater. Sci. (2000), https://doi.org/10.1146/annurev.matsci.30.1.159.

[39] J. Kennedy, P.P. Murmu, J. Leveneur, A. Markwitz, J. Futter, Controlling preferred orientation and electrical conductivity of zinc oxide thin films by post growth annealing treatment, Appl. Surf. Sci. 367 (2016) 52–58, https://doi.org/10.1016/j.apsusc.2016.01.160.

[40] Y. Kajikawa, Texture development of non-epitaxial polycrystalline ZnO films, J. Cryst. Growth 289 (2006) 387–394, https://doi.org/10.1016/j.jcrysgro.2005.11.089.

[41] Y.-H. Hu, Y.-C. Chen, H.-J. Xu, H. Gao, W.-H. Jiang, F. Hu, Y.-X. Wang, Texture ZnO thin-films and their application as front electrode in solar cells, Engineering 2 (2010) 973–978, https://doi.org/10.4236/eng.2010.212124.

[42] A.S. Lemine, O. Fayyaz, M. Yusuf, R.A. Shakoor, Z. Ahmad, J. Bhadra, N.J. Al-Thani, Microstructure and mechanical properties of aluminum matrix composites with bimodal-sized hybrid NbC-B4C reinforcements, Mater. Today Commun. 33 (2022) 104512, https://doi.org/10.1016/j.mtcomm.2022.104512.

[43] D. Viet Vu, D. Hai Le, C. Xuan Nguyen, T. Quang Trinh, Comparison of structural and electric properties of ZnO-based n-type thin films with different dopants for thermoelectric applications, J. Sol. Gel Sci. Technol. 91 (2019) 146–153, https://doi.org/10.1007/s10971-019-05024-0.

[44] J. Jancar, J.F. Douglas, F.W. Starr, S.K. Kumar, P. Cassagnau, A.J. Lesser, S.S. Sternstein, M.J. Buehler, Current issues in research on structure-property relationships in polymer nanocomposites, Polymer (Guildf). 51 (2010) 3321–3343, https://doi.org/10.1016/j.polymer.2010.04.074.

[45] X. Lou, S. Li, X. Chen, Q. Zhang, H. Deng, J. Zhang, D. Li, X. Zhang, Y. Zhang, H. Zeng, G. Tang, Lattice strain leads to high thermoelectric performance in polycrystalline SnSe, ACS Nano 15 (2021) 8204–8215, https://doi.org/10.1021/acsnano.1c01469.

[46] C. Zegadi, K. Abdelkebir, D. Chaumont, M. Adnane, S. Hamzaoui, Influence of Sn low doping on the morphological, structural and optical properties of ZnO films deposited by sol gel dip-coating, Adv. Mater. Phys. Chem. 4 (2014) 93–104, https://doi.org/10.4236/ampc.2014.45012.

[47] H. Long, A.A. Habeeb, D.M. Kinyua, K. Wang, B. Wang, P. Lu, Influences of ga doping on crystal structure and polarimetric pattern of SHG in ZnO nanofilms, Nanomaterials 9 (2019) 1–11, https://doi.org/10.3390/nano9060905.

[48] H. Ennaceri, M. Boujnah, D. Erfurt, J. Rappich, X. Lifei, A. Khaldoun, A. Benyoussef, A. Ennaoui, A. Taleb, Influence of stress on the photocatalytic properties of sprayed ZnO thin films, Sol. Energy Mater. Sol. Cells 201 (2019), https://doi.org/10.1016/j.solmat.2019.110058.

[49] M.F. Malek, M.H. Mamat, M.Z. Musa, Z. Khusaimi, M.Z. Sahdan, A.B. Suriani, A. Ishak, I. Saurdi, S.A. Rahman, M. Rusop, Thermal annealing-induced formation of ZnO nanoparticles: minimum strain and stress ameliorate preferred c-axis orientation and crystal-growth properties, J. Alloys Compd. 610 (2014) 575–588, https://doi.org/10.1016/j.jallcom.2014.05.036.

[50] M. Shaban, M. Zayed, H. Hamdy, Nanostructured ZnO thin films for self-cleaning applications, RSC Adv. 7 (2017) 617–631, https://doi.org/10.1039/c6ra24788a.

[51] A. Tuan Thanh Pham, P. Thanh Ngoc Vo, H. Kieu Thi Ta, N. Kim Pham, H. Thi Lai, H. Nhu Thi Tran, V. Cao Tran, T. Le Hoang Doan, S. Park, T. Bach Phan, Dopants and induced residual stress-controlled thermoelectric properties of ZnO thin films, Mater. Sci. Eng. B 261 (2020) 114712, https://doi.org/10.1016/j.mseb.2020.114712.

[52] I. Ozen, M.A. Gülgün, Residual stress relaxation and microstructure in ZnO thin films, 11th Int. Ceram. Congr. 45 (2006) 1316–1321, https://doi.org/10.4028/www.scientific.net/ast.45.1316.

[53] S. Saini, P. Mele, T. Oyake, J. Shiomi, J.P. Niemelä, M. Karppinen, K. Miyazaki, C. Li, T. Kawaharamura, A. Ichinose, L. Molina-Luna, Porosity-tuned thermal conductivity in thermoelectric Al-doped ZnO thin films grown by mist-chemical vapor deposition, Thin Solid Films 685 (2019) 180–185, https://doi.org/10.1016/j.tsf.2019.06.010.

[54] N.H. Tran Nguyen, T.H. Nguyen, Y.R. Liu, M. Aminzare, A.T.T. Pham, S. Cho, D.P. Wong, K.H. Chen, T. Seetawan, N.K. Pham, H.K.T. Ta, V.C. Tran, T.B. Phan, Thermoelectric properties of indium and gallium dually doped ZnO thin films, ACS Appl. Mater. Interfaces 8 (2016) 33916–33923, https://doi.org/10.1021/acsami.6b10591.

[55] S.S. Shinde, P.S. Shinde, Y.W. Oh, D. Haranath, C.H. Bhosale, K.Y. Rajpure, Structural, optoelectronic, luminescence and thermal properties of Ga-doped zinc oxide thin films, Appl. Surf. Sci. 258 (2012) 9969–9976, https://doi.org/10.1016/j.apsusc.2012.06.058.

[56] K.F. Cai, E. Müller, C. Drašar, A. Mrotzek, Preparation and thermoelectric properties of Al-doped ZnO ceramics, Mater. Sci. Eng. B 104 (2003) 45–48, https://doi.org/10.1016/S0921-5107(03)00280-0.

[57] W.C. Lim, J.P. Singh, Y. Kim, J. Song, K.H. Chae, T.Y. Seong, Effect of thermal annealing on the properties of ZnO thin films, Vacuum 183 (2021) 109776, https://doi.org/10.1016/j.vacuum.2020.109776.

[58] A. Raidou, M. Lharch, K. Nouneh, M. Aggour, A. Qachaou, L. Laanab, M. Fahoume, Effect of substrate on ZnO thin films grown by SILAR method, Proc. 2014 Int. Renew. Sustain. Energy Conf. IRSEC (2014) 695–700, https://doi.org/10.1109/IRSEC.2014.7059829, 2014.

[59] S. Mousavi, S. Davatolhagh, M. Moradi, Effects of thickness, impurity, surface roughness, and temperature on transport and thermoelectric coefficients of ultra-thin silicon nanowires: an analytic study, Phys. E Low-Dimensional Syst. Nanostructures. 118 (2020) 113889, https://doi.org/10.1016/j.physe.2019.113889.

[60] N. Baghdadi, N. Salah, A. Alshahrie, A.R. Ansari, K. Koumoto, The effect of morphological modification on the thermoelectric properties of ZnO nanomaterials, Ceram. Int. 47 (2021) 6169–6178, https://doi.org/10.1016/j.ceramint.2020.10.195.

[61] X. Wang, A. Lamantia, H. Jay, H. Sadeghi, C.J. Lambert, O.V. Kolosov, B.J. Robinson, Determination of electric and thermoelectric properties of molecular junctions by AFM in peak force tapping mode, Nanotechnology 34 (2023), https://doi.org/10.1088/1361-6528/acdf67.

[62] C.V. Manzano, B. Abad, M. Muñoz Rojo, Y.R. Koh, S.L. Hodson, A.M. Lopez Martinez, X. Xu, A. Shakouri, T.D. Sands, T. Borca-Tasciuc, M. Martin-Gonzalez, Anisotropic effects on the thermoelectric properties of highly oriented electrodeposited Bi2Te3 films, Sci. Rep. 6 (2016) 4–11, https://doi.org/10.1038/srep19129.

[63] S. Liu, M. Lan, G. Li, Y. Piao, H. Ahmoum, Q. Wang, Breaking the tradeoff among thermoelectric parameters by multi composite of porosity and CNT in AZO films, Energy 225 (2021) 120320, https://doi.org/10.1016/j.energy.2021.120320.

[64] S. Horike, T. Fukushima, T. Saito, T. Kuchimura, Y. Koshiba, M. Morimoto, K. Ishida, Highly stable n-type thermoelectric materials fabricated: via electron doping into inkjet-printed carbon nanotubes using oxygen-abundant simple polymers, Mol. Syst. Des. Eng. 2 (2017) 616–623, https://doi.org/10.1039/c7me00063d.

[65] K. Wan, Z. Liu, B.C. Schroeder, G. Chen, G. Santagiuliana, D.G. Papageorgiou, H. Zhang, E. Bilotti, Highly stretchable and sensitive self-powered sensors based on the N-Type thermoelectric effect of polyurethane/Nax(Ni-ett)n/graphene oxide composites, Compos. Commun. 28 (2021) 1–18, https://doi.org/10.1016/j.coco.2021.100952.

[66] N.P. Klochko, K.S. Klepikova, I.V. Khrypunova, D.O. Zhadan, S.I. Petrushenko, V.R. Kopach, S.V. Dukarov, V.M. Sukhov, M.V. Kirichenko, A.L. Khrypunova, Flexible thermoelectric module based on zinc oxide thin film grown via SILAR, Curr. Appl. Phys. 21 (2021) 121–133, https://doi.org/10.1016/j.cap.2020.10.012.

[67] B.W. Stuart, K. Morgan, X. Tao, I. Zeimpekis, Z. Feng, D. Gregory, H.E. Assender, Linear electron beam assisted roll-to-roll in-vacuum flexographic patterning for flexible thermoelectric generators, Coatings 11 (2021) 1–14, https://doi.org/10.3390/COATINGS11121470.

[68] S. Liu, S. Peng, J. Ma, G. Li, X. Qin, M. Li, Q. Wang, Structure and thermoelectric properties of Al-doped ZnO films prepared by thermal oxidization under high magnetic field, Superlattices Microstruct 104 (2017) 282–290, https://doi.org/10.1016/j.spmi.2017.02.034.

[69] K. Ankireddy, A.K. Menon, B. Iezzi, S.K. Yee, M.D. Losego, J.S. Jur, Electrical conductivity, thermal behavior, and Seebeck coefficient of conductive films for printed thermoelectric energy harvesting systems, J. Electron. Mater. 45 (2016) 5561–5569, https://doi.org/10.1007/s11664-016-4780-2.

[70] C. Archana, S. Harish, R. Abinaya, J. Archana, M. Navaneethan, Interface modified MoS2/CNT with enhanced power factor via energy filtering effect for flexible thermoelectric applications, Sensors Actuators A Phys 348 (2022) 113938, https://doi.org/10.1016/j.sna.2022.113938.

[71] A.K. Menon, O. Meek, A.J. Eng, S.K. Yee, Radial thermoelectric generator fabricated from n- and p-type conducting polymers, J. Appl. Polym. Sci. 134 (2017) 1–8, https://doi.org/10.1002/app.44060.

[72] A. Abd-Elsalam, H.O. Badr, A.A. Abdel-Rehim, I.S. El-Mahallawi, Structure and thermoelectric behavior of polyaniline-based/CNT-composite, Curr. Appl. Phys. 36 (2022) 88–92, https://doi.org/10.1016/j.cap.2021.11.012.

[73] K. Suemori, S. Hoshino, T. Kamata, Flexible and lightweight thermoelectric generators composed of carbon nanotube-polystyrene composites printed on film substrate, Appl. Phys. Lett. 103 (2013), https://doi.org/10.1063/1.4824648.

[74] S. Hu, S. Zeng, X. Li, J. Jiang, W. Yang, Y. Chen, M. Li, J. Zheng, Flexible and high performance of n-type thermoelectric PVDF composite film induced by nickel nanowires, Mater. Des. 188 (2020) 108496, https://doi.org/10.1016/j.matdes.2020.108496.

[75] C. Awasthi, R. Meena, A. Kandasami, S.S. Islam, Structural and thermoelectric properties of MoSe2/CNT nanocomposites, J. Phys. Chem. Solids. 184 (2024), https://doi.org/10.1016/j.jpcs.2023.111726.

[76] J. He, M.G. Kanatzidis, V.P. Dravid, High performance bulk thermoelectrics via a panoscopic approach, Mater. Today 16 (2013) 166–176, https://doi.org/10.1016/j.mattod.2013.05.004.

[77] B. Zhou, L. Chen, C. Li, N. Qi, Z. Chen, X. Su, X.F. Tang, Significant enhancement in the thermoelectric performance of aluminum-doped ZnO tuned by pore structure, ACS Appl. Mater. Interfaces 12 (2020) 51669–51678, https://doi.org/10.1021/acsami.0c16506.

[78] V. Pandiyarasan, S. Suhasini, J. Archana, M. Navaneethan, A. Majumdar, Y. Hayakawa, H. Ikeda, Fabrication of hierarchical ZnO nanostructures on cotton fabric for wearable device applications, Appl. Surf. Sci. 418 (2017) 352–361, https://doi.org/10.1016/j.apsusc.2016.12.202.

[79] E. Redel, H. Baumgart, Thermoelectric porous MOF based hybrid materials, Apl. Mater. 8 (2020) 1–10, https://doi.org/10.1063/5.0004699.

[80] T. Ishibe, A. Tomeda, K. Watanabe, Y. Kamakura, N. Mori, N. Naruse, Y. Mera, Y. Yamashita, Y. Nakamura, Methodology of thermoelectric power factor enhancement by controlling nanowire interface, ACS Appl. Mater. Interfaces 10 (2018) 37709–37716, https://doi.org/10.1021/acsami.8b13528.

[81] J. Loureiro, N. Neves, R. Barros, T. Mateus, R. Santos, S. Filonovich, S. Reparaz, C.M. Sotomayor-Torres, F. Wyczisk, L. Divay, R. Martins, I. Ferreira, Transparent aluminium zinc oxide thin films with enhanced thermoelectric properties, J. Mater. Chem. A. 2 (2014) 6649–6655, https://doi.org/10.1039/c3ta15052f.

[82] K.H. Jung, K. Hyoung Lee, W.S. Seo, S.M. Choi, An enhancement of a thermoelectric power factor in a Ga-doped ZnO system: a chemical compression by enlarged Ga solubility, Appl. Phys. Lett. 100 (2012) 2010–2014, https://doi.org/10.1063/1.4729560.